



High efficiency for H₂ evolution and NO removal over the Ag nanoparticles bridged g-C₃N₄ and WS₂ heterojunction photocatalysts

Yongning Ma^a, Juan Li^{a,d}, Enzhou Liu^{a,b,c}, Jun Wan^a, Xiaoyun Hu^{b,*}, Jun Fan^{a,*}

^a School of Chemical Engineering, Northwest University, Xi'an, 710069, PR China

^b School of Physics, Northwest University, Xi'an, 710069, PR China

^c Institute of Modern Physics, Northwest University, Xi'an, 710069, PR China

^d School of Environmental Engineering and Chemistry, Luoyang Institute of Science and Technology, Luoyang, 471023, PR China



ARTICLE INFO

Article history:

Received 20 March 2017

Received in revised form 13 July 2017

Accepted 23 July 2017

Available online 24 July 2017

Keywords:

Photocatalysis

H₂ production

NO removal

Bridged structure

g-C₃N₄

ABSTRACT

Ag nanoparticles bridged g-C₃N₄ and WS₂ nanosheets heterojunction (x-y-WAC) and Ag nanoparticles deposited g-C₃N₄/WS₂ heterojunction (x-y-AWCA) were prepared through a solvent evaporation and high temperature calcinations method, the x is the percentage of Ag nanoparticles and y is WS₂ nanosheets in mass fraction, respectively. The as-prepared heterojunctions were applied to water splitting for H₂ evolution and NO removal at the indoor air level under simulated sunlight irradiation, in which the H₂ production rate and NO removal efficiency of the bridged structure are much higher than that of deposited structure. The H₂ production rate of most effective samples (2-20-WAC) were measured to be 68.62 $\mu\text{mol h}^{-1}$, which are 1.86 and 15.67 times higher than that of pure g-C₃N₄ and WS₂ nanosheets, respectively. The gradient test of Ag nanoparticles and WS₂ nanosheets indicated that the optimum amounts of Ag nanoparticles and WS₂ nanosheets were 2% and 20% in mass fraction. The morphology of 2-20-WAC heterojunction was characterized by SEM, TEM and HRTEM techniques and the results revealed that the Ag nanoparticles were intercalated into the interlayer of g-C₃N₄ and WS₂ nanosheets. According to the XRD, FT-IR, UV-vis and XPS analysis, the Ag nanoparticles, g-C₃N₄ and WS₂ nanosheets are hybrid by chemical bond through the second calcinations. Furthermore, the bridged structure can promote the separation rate of charge carriers and suppress the recombination of them at the same time, which could be deduced from photocurrent and PL investigation. Based on the characterization and results analysis, it can be inferred that the bridged structure can accelerate the transport of charge carriers and restrain the recombination of electrons and holes at the same time, which could improve photocatalytic performance of the heterojunction.

© 2017 Elsevier B.V. All rights reserved.

1. Introduction

Energy shortage and environment pollution are unavoidable problems in recent years and puzzled the researchers all over the worlds [1–3]. The renewable energies, such as nuclear energy, wind energy and solar energy, are all good candidates to supply the shortage of fossil energy and alleviate the environment pollution [4,5]. In varies renewable energies, solar energy is the most potential one because it have many merits compared with others, such as widely existed, environment friendly, no toxic gases emission. However, the storage of solar energy is the most obstacles on the practical application, which had been regarded as the most effective ways to relieve the energy shortage and environ-

mental deterioration. To address the problems, some researchers devoted to the H₂ generation from water splitting and noxious gas removal at the indoor air level under sunlight irradiation with photocatalyst exist in the reaction system and the photoreaction process has not any toxic substances production and gas emission, which is an ideal project to convert solar energy to chemical energy and eliminate the environmental pollution [6–9]. Graphitic carbon nitride (g-C₃N₄), a potential photocatalyst to address the energy shortage and environmental pollution, has a proper conduction band ($E_{CB} = -1.12$ eV) for H₂ ($\Phi_{H+/H2} = 0$ eV) generation and a positive valance band ($E_{VB} = 1.53$ eV) for NO removal under sunlight irradiation [10–13]. Moreover, the structure of g-C₃N₄ with π -conjugated graphitic planes formed by triazine units makes it have many promising properties, such as metal-free, good chemical stability and photoelectric properties [14–16]. Besides, the pristine g-C₃N₄ are stacked by layered g-C₃N₄ nanosheets with the lattice space in the planes are measured about 0.34 nm and

* Corresponding authors.

E-mail addresses: hxy3275@nwu.edu.cn (X. Hu), fanjun@nwu.edu.cn (J. Fan).

the distance of interlayer are about 0.67 nm, which are benefits for the transport of charge carriers in the planes [4]. Based on above, most of the active sites are distributed on the edges of pristine g-C₃N₄ and the performance limited by the less quantity of active sites. Therefore, many researchers have devoted to exfoliate the pristine g-C₃N₄ to g-C₃N₄ nanosheets with more active sites exposure, which can make the charge carriers transferred to the surface of g-C₃N₄ nanosheets rapidly [17,18]. Additionally, the ultrathin g-C₃N₄ has many intriguing properties different from bulk g-C₃N₄ and present potential in diverse applications due to the decreased transport distance of charge carriers [19,20]. However, the fast recombination of photo-generated electron-hole pairs and the re-stack of g-C₃N₄ nanosheets have a negative impact on the performances of H₂ generation and NO removal [21–24].

To solve the problems mentioned above, many strategies have been made to accelerate the transfer rate of charge carriers and restrain the recombination of electrons and holes [25]. Typically, the Nobel metals (Pt, Au, and Ag) deposited on the surface of g-C₃N₄ [19,26,27], metallic oxide semiconductors (TiO₂ [28], ZnO [29], Al₂O₃ [30], WO₃ [31] and Fe₂O₃ [32]) hybrid with g-C₃N₄ are effective measures to suppress the recombination of electrons and holes. Additionally, the establishment of two-dimensions heterogeneous is the most promising project to improve the separation rate and suppress the recombination of electrons and holes at the same time due to the big contact areas [33–35]. The WS₂, a promising two-dimension material which can absorb the light in the whole band gap, is individual S-W-S layers weakly interact with each other and the band gap is an indirect-to-direct semiconductor from bulk to few layer [36–38]. Moreover, the good conductivity of WS₂ nanosheets can make the electrons transport from interiors to the surface quickly [39]. Therefore, the establishment of WS₂ and g-C₃N₄ heterojunction is a feasible program to improve the conversion rate of light energy and accelerate the transport of electrons simultaneously. Yu [40] and co-workers had been applied g-C₃N₄/WS₂ heterogeneous in H₂ production and the reported H₂ production rate was 1.3 times higher than that of conventional Pt as a co-catalyst at the same loading amount. Wang [41] and co-workers loaded WS₂ nanosheets on g-C₃N₄ nanosheets as co-catalyst and used as electrode materials, the investigation result indicated that the WS₂/mpg-CN/FTO electrode shows the enhanced potential in photocatalytic water splitting system. However, the transport of charge carriers between the interface of CNN and WSN was restrained because the interface effect [42]. Therefore, a two-dimension heterojunction with bridged structure (Ag nanoparticles bridged WS₂ and g-C₃N₄ nanosheets) are proposed in this article to accelerate the transport speed of electrons. Additionally, the heterojunction with bridged structure had never been reported and the photocatalytic mechanism of this structure is ambiguous so far. Herein, to build the heterojunction with bridge structure and study the photocatalytic mechanism of them are interesting and meaningful.

Based on predecessor researchers, we build two types of heterojunctions, Ag nanoparticles bridged WS₂ and g-C₃N₄ nanosheets (x-y-WAC) and Ag nanoparticles deposited on the surface of WS₂ and g-C₃N₄ heterojunction (x-y-AWCA), via a solvent evaporation and high temperature calcinations process. In x-y-WAC and x-y-AWCA samples, the x is the percentage of Ag nanoparticles in mass fraction and y represent that of WS₂ nanosheets. The photocatalytic performance of both types heterojunction are evaluated by water splitting for H₂ evolution and NO removal at the indoor air level under simulated sunlight irradiation. The traditional Ag/g-C₃N₄ heterojunction and WS₂/g-C₃N₄ heterojunction are abbreviated to x-ACNN and y-WSCN, respectively. The x and y represent the percentage of Ag nanoparticles and WS₂ nanosheets, respectively.

Besides, the g-C₃N₄ nanosheets and WS₂ nanosheets are simplified to CNN and WSN, respectively.

2. Experimental section

2.1. Photocatalytic H₂ evolution from water splitting

The performance of H₂ production on different photocatalysts was carried out in a Pyrex top-irradiation reaction vessel connected to a glass-closed gas circulation system. For each reaction, 0.1 g catalyst powder was dispersed in water (100 mL) containing triethanolamine (TEOA 10 vol%) as sacrificial and 3 wt% Pt was photo-deposited on the catalysts using the H₂PtCl₆ dissolved in the reactant solution. The reactant solution was vacuumized to remove air completely prior to irradiation under a 300 W Xe lamp and the amount of H₂ was detected every 60 min, the reaction time was started after 30 min irradiation and vacuumized again for each samples. The evolved gas was analyzed by gas chromatography equipped with a thermal conductive detector (TCD) with nitrogen as the carrier gas.

2.2. Photocatalytic removal of NO

The photocatalytic removal rate of NO was performed at ambient temperature in a continuous flowing reactor [43,44]. For each experiment, 0.1 g catalyst powder was dispersed in the center of the reactor by a dish with a diameter of 6.5 cm. The reactant gas (the concentration of NO was 2.76 ppm) was fed into the reactor with a total flow rate in 400 mL min⁻¹, and the residence time of mixture gas in the reaction vessel was about 10 s. After reached to the adsorption–desorption equilibrium, a 300 W xenon lamp (Microsolar 300) was used as simulated light sources (the schematic diagram of the photocatalytic degradation set-up shown in Fig.S1). The concentration of NO was continuously measured by an electrochemical NO analyzer (Shenzhen Jishunan Technology CO. LTD., JSA9-NO). The NO conversion (η) was calculated as: $\eta(\%) = (1 - C/C_0) \times 100\%$, where C is the outlet concentration of NO after reaction for time t, and C₀ represents the inlet concentration after achieving the adsorption–desorption equilibrium.

3. Results and discussion

3.1. Characterization

The phase structures and crystals were carried out by XRD analysis and the results shown in Fig. 1. For pure samples of bulk g-C₃N₄ and CNN, the weak and broad peak at 13.5° correspond to the (100) plane and the strong and sharp peak at 27.5° correspond to the (002) planes [41], which can be good accordance with the graphitic carbon nitride [45]. The peak intensity at 27.5° are decreased obviously, which can be owned to the expanded interlayer distance of (002) planes in the ultrasonic process. The diffraction pattern of pure WSN shows distinctly peaks at 14.3°, 28.8°, 33.6°, 39.5°, 43.9°, 49.7°, 58.4° and 62.6°, which correspond to the planes (002), (004), (101), (103), (006), (105), (110) and (107) in the (JCPDS 02-0131), respectively. In composites, the typical peaks of CNN at 27.5° and WSN at 14.3° and 33.6° can be found in the as prepared 20-WSCN composites, which indicated that the exfoliated CNN had been composited with WSN uniformly. It is well known that a narrow and strong peak at 27.5° correspond to a small interlayer distance of g-C₃N₄ [45]. Therefore, the peak intensity at 27.5° was decreased in 20-WSCN composite indicated that the exfoliated CNN was well composited with WSN rather than itself. A new peak at 23.7° (the green dash region in Fig. 1) can be found when the composites was constantly heated 120 min at 400 °C condition, which may be

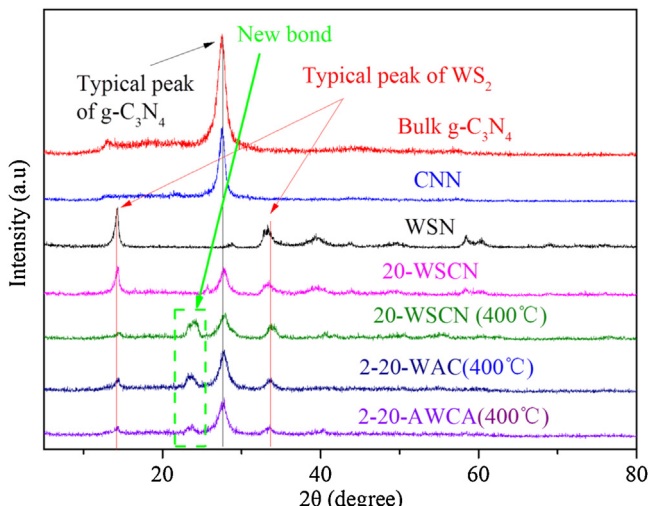


Fig. 1. The X-ray diffraction patterns of different samples.

caused by the formation of new chemical bond between interface of CNN and WSN (certified by the FT-IR spectra in Fig.S2). Based on above analysis results, it can be concluded that the 20-WSCN composite was converted to heterojunction through 400 °C calcinations. Therefore, the heterojunctions of 2-20-WAC and 2-20-AWCA were also prepared by the solvent evaporation and high temperature calcinations process. In XRD patterns, it can be seen the peaks of 2-20-WAC and 2-20-AWCA heterojunction are similar to that of 20-WSCN heterojunction, which indicated that the Ag nanoparticles and WSN are hybridized with CNN by chemical bond. The peaks of Ag nanoparticles are not found in the XRD pattern, which may be caused by the insufficient amount of Ag nanoparticles and the existed of Ag nanoparticles can be proved by TEM analysis and XPS spectrum. Herein, it can be conclude that the 2-20-WAC and 2-20-AWCA heterojunction are established by the solvent evaporation and high temperature calcinations process, which was further analyzed in morphology characterization and XPS spectra.

The morphology of samples was characterized by SEM, TEM and HRTEM and the results shown in Fig. 2. The SEM images of bulk WS₂ and g-C₃N₄ are exhibited in Fig. 2a and b, respectively. It can be seen that both the structure of bulk WS₂ and g-C₃N₄ are stacked by layer materials and the size of them are about 200 nm. The SEM analysis indicated that the bulk WS₂ and g-C₃N₄ can exfoliate to ultra-thin nanosheets with few layer structure or single layer structure and some researchers had been exfoliated it to nanosheets [46,47]. Fig. 2c and d are TEM images of 2-20-WAC sample. The red dashed lines (Fig. 2c) are the edges of WSN and the black points rounded by luminous yellow dashed lines are Ag nanoparticles. The WSN are covered on the surface of CNN and the un-intercalated Ag nanoparticles were deposited on the surface of CNN can also be found in the images. The vague black points in Fig. 2d are Ag nanoparticles, which indicated that the WSN are covered on the Ag nanoparticles and CNN. The analysis of Fig. 2c and d indicated that the Ag nanoparticles are sandwiched between WSN and CNN. To prove the black points and the covered nanosheets are Ag nanoparticles and WS₂, respectively. HRTEM investigation was employed and the results can be seen in Fig. 2e and f. Fig. 2e is the HRTEM of WSN in the 20-WSCN heterojunction, the lattice distance of WSN is about 0.61 nm which correspond to the (002) plane of WSN (JCPDS 02-0131) and the size of the nanosheets are larger than 20 nm. The HRTEM of Ag nanoparticles (Fig. 2f) revealed that the lattice distance of Ag nanoparticles is about 0.24 nm (correspond to the (111) plane of Ag) and the size of Ag nanoparticles is about 15–20 nm. Moreover, the zeta potential (Fig.S3) of CNN, 2-ACNN and WSN were measure to be -17.9 mV, +5.6 mV and -23.4 mV, respectively. The results

revealed that the 2-ACNN and WSN had an opposite value of Zeta potential, which indicated the 2-ACNN will be good composed with WSN but not re-associated with itself. To exhibit the different structure of 2-20-WAC and 2-20-AWCA further, the TEM images of 2-20-AWCA are shown in Fig. 2g and h. In the images, the sizes of Ag nanoparticles and WSN are similar to that of 2-20-WAC and the exposed Ag nanoparticles can be seen distinctly, which certified that the Ag nanoparticles of 2-20-AWCA were deposited on the surface of WSN and CNN heterojunction but not intercalated into the interlayer of WSN and CNN. According to TEM analysis, it can be concluded that the Ag nanoparticles are intercalated into the interlayer space of WSN and CNN.

Moreover, the mapping images (corresponding to the SEM of 2-20-WAC heterojunction in (Fig. 3a) of C, N, Ag, W and S specials were carried out to prove the Ag nanoparticles intercalated into the interlayer of CNN and WSN. Fig. 3a is the SEM image of 2-20-WAC heterojunction, it can be seen some light line and dark line arranged in turns (see the region enclosed by red dash line in Fig. 3a). The light lines maybe the edges of WSN and CNN in the 2-20-WAC heterojunction and the dark lines is the layers distance of WSN and CNN. Therefore, it can be conclude that the Ag nanoparticles were intercalated into the interlayer of WSN and CNN, which expanded the interlayer distance of as prepared samples. Besides, the mapping images of C, N, Ag, W and S specials (based on the SEM of 2-20-WAC in Fig. 3a) were also used to certify the Ag nanoparticles intercalated into the interlayer of samples and the results exhibited in Fig. 3b, c, d, e and f, respectively. It can be seen the C, N, Ag, W and S specials were dispersed uniformly in the 2-20-WAC heterojunction. So, it can be inferred that the Ag nanoparticles were intercalated into the interlayers of WSN and CNN.

The FT-IR spectra of WSN, 20-WSCN, 2-20-AWCA, 2-20-WAC and CNN are shown in Fig. 4. For CNN, the peaks between 1634 cm⁻¹ and 1238 cm⁻¹ are attributed to the typical stretching modes of C–N heterocycles, and the peaks around 807 cm⁻¹ is the characteristic breathing mode of triazine units. The broad band between 2800 and 3400 cm⁻¹ are due to the uncondensed terminal amino groups (–NH₂ or =NH) at the defect sites of aromatic ring [48]. For pure WS₂ nanosheets, there are no distinct peaks in the range of 600–4000 cm⁻¹ [40]. For 20-WSCN, 2-20-AWCA, 2-20-WAC heterojunctions, the peaks intensity at 1394 cm⁻¹, 1316 cm⁻¹ and 1236 cm⁻¹ are decreased, which can be attributed to the fact that the black WSN can absorb the infrared light [40]. Besides, the broad peaks between 2800 and 3400 cm⁻¹ are also decreased with the incorporation of WS₂ nanosheets, which can be owned to the hybridized WSN and Ag nanoparticles restrict the vibration of uncondensed terminal amino groups on the surface of CNN. Additionally, the new peaks in the 2-20-WAC heterojunction (heated to 400 °C) can be found in the FT-IR spectra (Fig.S2), which indicated that the new chemical bond was formatted while the composites was heated to 400 °C. The Ag nanoparticles were not detected in 2-20-AWCA and 2-20-WAC samples, which can also be attributed to the less content of Ag nanoparticles. However, the existence of Ag nanoparticles had been proved by TEM (Fig. 2) characterization and will be further confirmed by XPS analysis (Fig. 6).

The UV-vis absorption spectra show in Figs. 5. The absorption property of bulk g-C₃N₄, CNN, WSN, 10-WSCN, 20-WSCN, 30-WSCN, and 20-WSCN (400 °C) are exhibited in Fig. 5a. It can be seen from the spectra, the absorption edge of bulk g-C₃N₄ is located at 460 nm and the band gap was estimated to be about 2.70 eV according to the absorption edge of bulk g-C₃N₄. When the bulk g-C₃N₄ exfoliated to CNN, the absorption edge was shifted to shortwave and the calculated band gap reached to 2.82 eV (Fig.S4a) because of the quantum size effect [46]. For WSN, it has a very strong absorption intensity in whole absorption band (1.95 eV), which is the good candidate to convert solar energy to chemical energy in theory. Moreover, the VB (valence band) of CNN and WSN

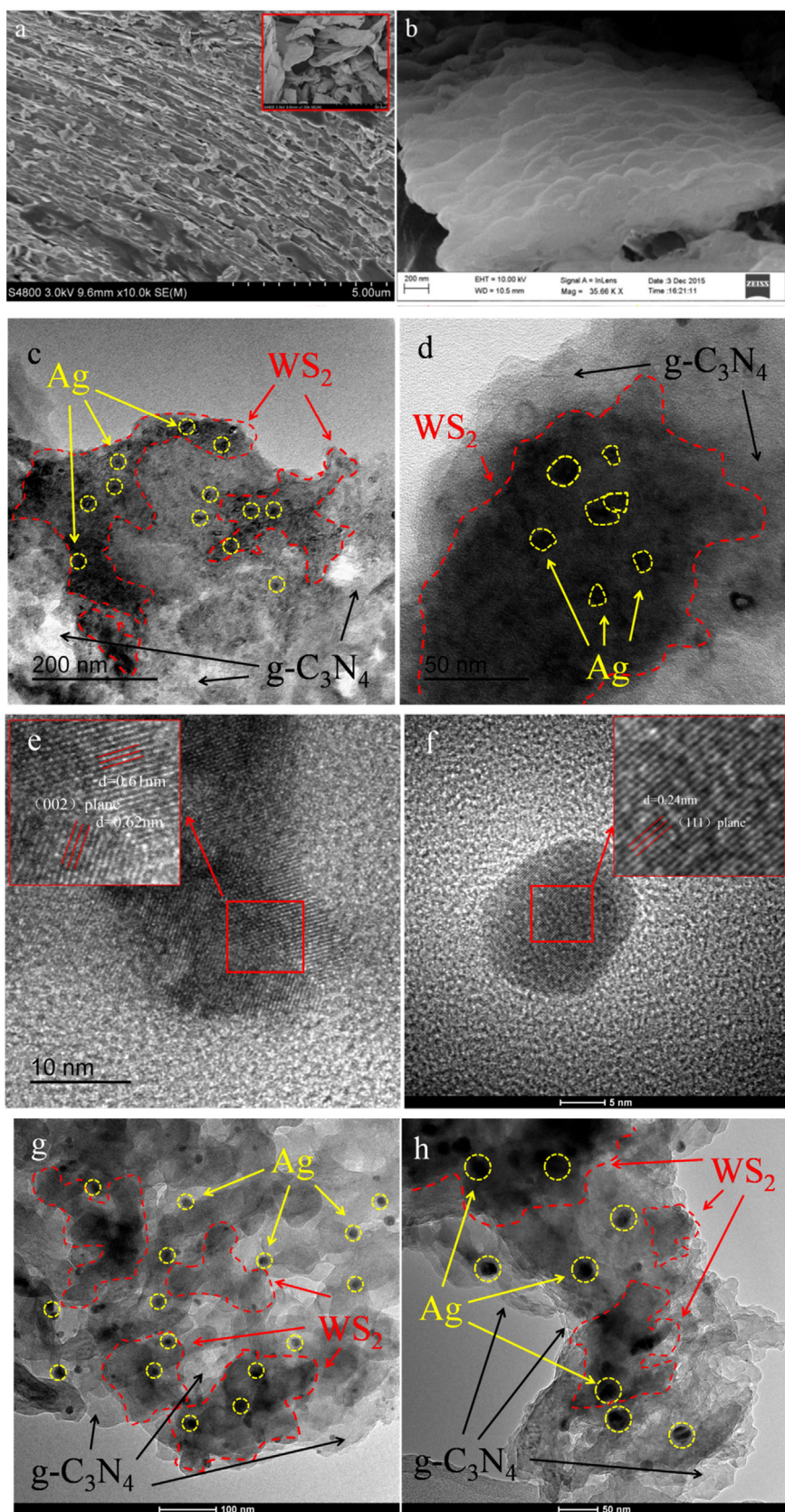


Fig. 2. The SEM images of bulk WS_2 (a) and bulk $g\text{-}C_3N_4$ (b), TEM images of 2-20-WAC (c-d), HRTEM of WSN in 20-WSCN (e) and Ag nanoparticles in 2-ACNN (f), TEM images of 2-20-AWCA (g-h).

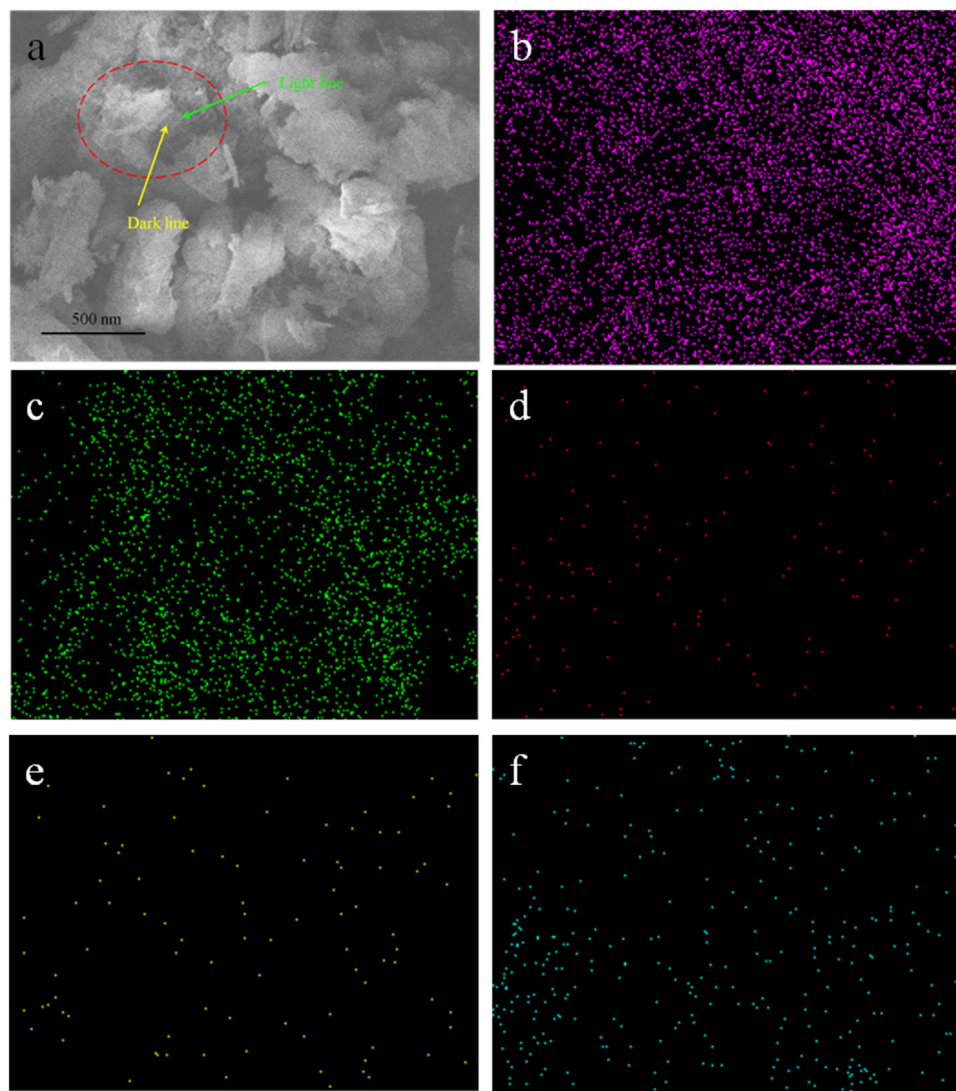


Fig. 3. The SEM images of 2-20-WAC (a) and the corresponding mapping images of C (b), N (c), Ag (d), W (e) and S (f) species.

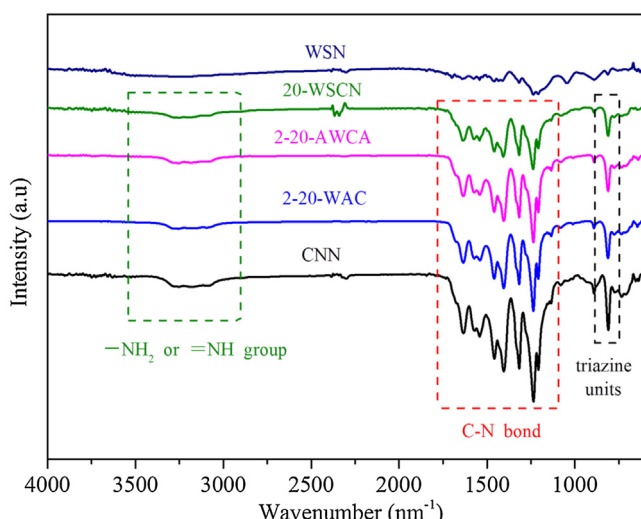


Fig. 4. The FT-IR spectra of samples.

was estimated to +1.65 eV and +1.63 eV according to the XPS spectra (Fig.S4b), respectively. The absorption intensity at the range of visible light are enhanced with the increase of the WSN and the band gap of 10-WSCN, 20-WSCN and 30-WSCN is decreased to 2.58 eV, 2.53 eV and 1.98 eV, respectively. However, the band gap of 20-WSCN was increased to 2.99 eV after heated at 400 °C. Fig. 5b is the UV-vis spectrum of bulk g-C₃N₄, CNN, 20-WSCN, 2-20-AWCA and 2-20-WAC heterojunctions. The absorption properties of 20-WSCN, 2-20-WAC and 2-20-AWCA heterojunctions are negative than that of 20-WSCN, 2-20-WAC and 2-20-AWCA composites (without heated at 400 °C). For heterojunctions, the absorption intensity of 20-WSCN are similar to that of 2-20-AWCA because the main contacted surface of them are WSN and CNN. However, the absorption intensity of 2-20-WAC heterojunction is negative than that of 20-WSCN and 2-20-AWCA heterojunctions, which may be caused by the expanded interlayer distance. The analysis of UV-vis absorption spectra further revealed that the heterojunctions can be prepared in the calcinations process and the absorption intensity of heterojunction in the visible light region can be improved with hybridization of WSN.

The elemental composition and chemical status of 2-20-WAC were characterized by X-ray photoelectron spectroscopy (XPS) and the results exhibited in Fig. 6. The C, N, O, Ag, S and W species can

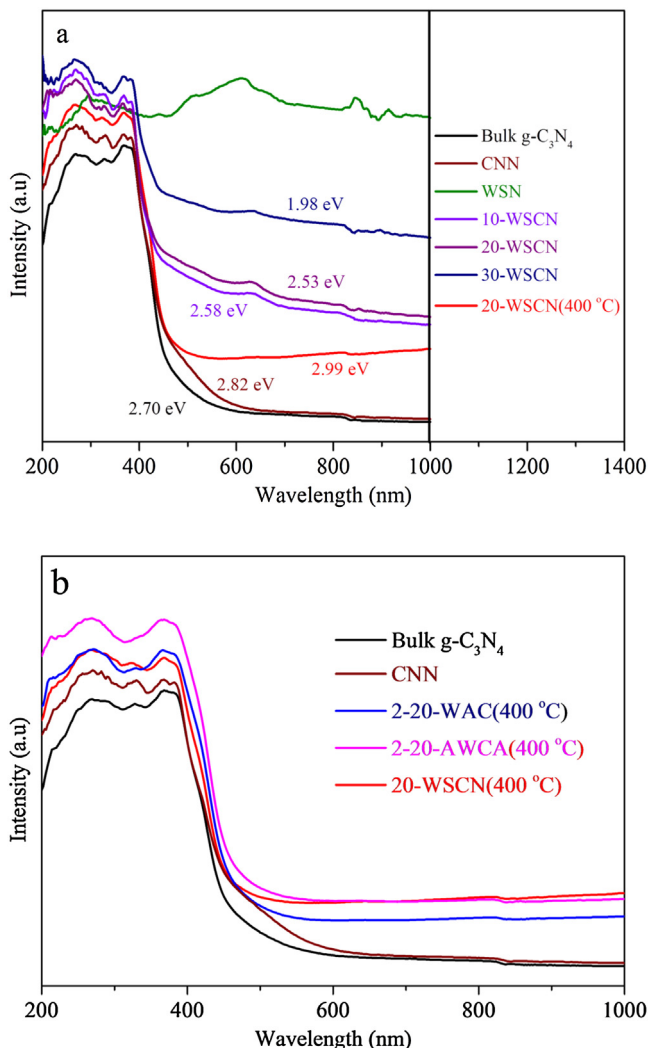


Fig. 5. The UV-vis spectra of $\text{g-C}_3\text{N}_4$, WS_2 and WSCN composites (a). The UV-vis spectra of heterojunctions with different structure (b).

be found in the survey spectrum (Fig. 6a), which indicated that the WSN, CNN and Ag nanoparticles are hybridized in the 2-20-WAC sample. In Fig. 6b, it can be observed the peak of W4f has three characteristic peaks at binding energies of 30.2 eV, 32.6 eV and 34.9 eV. The peaks at 30.2 eV and 32.6 eV can be ascribed to the W^{4+} species [41] and the peaks at higher binding energies can be attributed to W^{6+} species which was oxidized in the second calcinations process. Considering the analysis results of S2p (Fig. 6c) and Ag3d (Fig. 6d), it can be inferred that the Ag nanoparticles and WSN are hybridized with CNN. The existence of W^{6+} may be caused by the oxidation reaction of WS_2 in the hybridize process and the lower binding energy shifts revealed that a strong chemical interaction included in the W species and the conjugation [49]. As shown in Fig. 6d, the peaks of Ag 3d5/2 and Ag 3d3/2 are located at 365.0 eV and 371.0 eV, respectively. The peak at 371.0 eV can be assigned to metallic Ag^0 species while the peaks at 365.0 eV is assigned to Ag^+ species which was originated the AgNO_3 and combined with CNN, WSN or the residual oxidation group on the surface of samples [50]. Moreover, the XPS spectra of C1s and N1s in the pristine $\text{g-C}_3\text{N}_4$ and 2-20-WAC heterojunction were also investigated to prove the Ag nanoparticles intercalated into the interlayer of CNN and WSN. The results exhibited in Fig. 6e and f. For the peaks of C1s (Fig. 6e) in the pristine $\text{g-C}_3\text{N}_4$, the peaks located at 285.2 eV, 283.5 eV and 282.1 eV can be attributed to the bond energy of C–C, C=N and C–N

[1,5], respectively. The XPS spectra of C1s in 2-20-WAC heterojunction are similar to that of pristine $\text{g-C}_3\text{N}_4$, which indicated that the main structure of CNN was not destroyed in the composite process. For the N1s (Fig. 6f) in the pristine $\text{g-C}_3\text{N}_4$, the peaks located at 400.8 eV, 399.8 eV and 398.4 eV can be attributed to the bond energy of C–N–H, N–(C)₃ and C=N–C [22], respectively. Different with the spectra of C1s, the peak of N1s at 399.8 eV was shifted to about 399.0 eV in the 2-20-WAC heterojunction, which may be caused by the interactions of Ag nanoparticles and CNN lead to the photo-induced electrons (generated from CNN) transported to the Ag nanoparticles easily. Based on above analysis, it is reasonable to consider that the 2-20-WAC heterojunction with bridged structure was synthesized.

3.2. Photocatalytic results and analysis

The photocatalytic performance of various samples was firstly evaluated by H_2 evolution from water splitting under simulated sunlight irradiation using TEOA (triethanolamine) as a scavenger. The control experiments indicated that there are no hydrogen can be detected in the absence of either irradiation or photocatalyst, suggesting the H_2 evolution is a photocatalytic process. Fig. 7a depicts the performance of bulk $\text{g-C}_3\text{N}_4$, CNN, WSN and CdS samples on H_2 production. The H_2 production rate of bulk $\text{g-C}_3\text{N}_4$ was $27.06 \mu\text{mol h}^{-1}$ and that of CNN, WSN and CdS are $36.86 \mu\text{mol h}^{-1}$, $4.38 \mu\text{mol h}^{-1}$ and $9.04 \mu\text{mol h}^{-1}$, respectively. The results revealed that the CNN is the most suitable candidate to split water for H_2 generation. Therefore, to modify the CNN for the improvement of H_2 production is a significantly project to enhance the photocatalytic performance. Fig. 7b is the comparison performance of CNN, 2-ACNN, 20-WSCN, 2-20-AWCA and 2-20-WAC samples. The H_2 production rate of 2-20-WAC is $68.62 \mu\text{mol h}^{-1}$ and the rate of pure CNN is only $36.86 \mu\text{mol h}^{-1}$. In Fig. 7b, the performance of 2-ACNN, 20-WSCN and 2-20-AWCA was weaker than that of 2-20-WAC and the rate of H_2 production are $53.69 \mu\text{mol h}^{-1}$, $45.81 \mu\text{mol h}^{-1}$ and $21.25 \mu\text{mol h}^{-1}$, respectively. To illustrate the performance of heterojunction with bridged structure are better than that of traditional two-dimension heterojunction, the H_2 production rate of y-WSCN (Fig.5a) and x-ACNN (Fig.5b) were also investigated. The Fig.5a indicated that the H_2 production rate of 10-WSCN, 20-WSCN and 30-WSCN are $39.91 \mu\text{mol h}^{-1}$, $45.81 \mu\text{mol h}^{-1}$ and $32.74 \mu\text{mol h}^{-1}$, respectively. The H_2 production rate of 1-ACNN, 2-ACNN, 3-ACNN, 4-ACNN and 5-ACNN are $26.89 \mu\text{mol h}^{-1}$, $53.69 \mu\text{mol h}^{-1}$, $24.06 \mu\text{mol h}^{-1}$, $19.45 \mu\text{mol h}^{-1}$ and $9.98 \mu\text{mol h}^{-1}$, respectively. The experiments results revealed that the heterojunction with bridged structure have an excellent performance than that of traditional heterojunction and the optimum amount of Ag and WSN are 2% and 20%, respectively. The degraded performance of 30-WSCN, 3-ACNN, 4-ACNN and 5-ACNN on H_2 production can be owned to the excessive amount of Ag nanoparticles and WSN agglomerated and covered on the active sites of CNN. Moreover, the performance of deposited structure was poorer than that of bridged structure. Besides, the performance of Ag^+ in the heterojunction reduced by H_2O_2 , NaBH_4 and simulated sunlight irradiation are also investigated and the results (Fig.6) indicated the simulated sunlight irradiation is the most appropriate method. The H_2 production rate of 1-ACNN, 2-ACNN and 3-ACNN were decreased to $21.06 \mu\text{mol h}^{-1}$, $32.38 \mu\text{mol h}^{-1}$, $27.45 \mu\text{mol h}^{-1}$ when the Ag^+ reduced by H_2O_2 (Fig.6a) and the H_2 production rate are decreased to $13.33 \mu\text{mol h}^{-1}$, $19.42 \mu\text{mol h}^{-1}$, $15.59 \mu\text{mol h}^{-1}$ after the reduction reaction of NaBH_4 (Fig.6b). The degraded performance of heterojunction can be attributed to the by-products in the reduction process covered on the surface of Ag nanoparticles and restrained the transport of charge carries. On the other hand, the active sites of heterojunction may be destroyed by the H_2O_2 and NaBH_4 because the powerful reducing power. Based on the

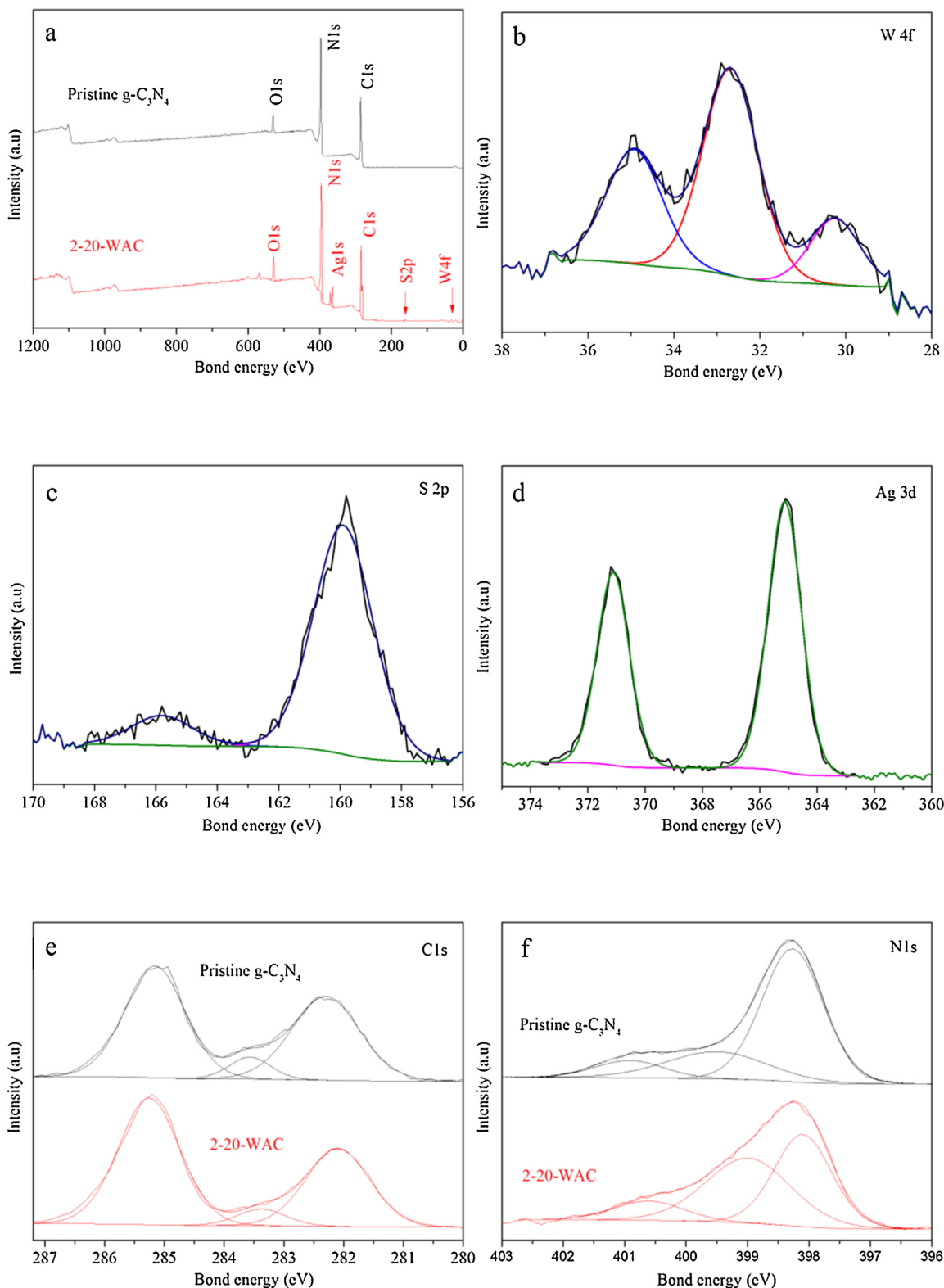


Fig. 6. The XPS spectrum of 2-20-WAC samples in survey (a), W4f (b), S2p (c), Ag 3d (d), C1s (e) and N1s (f) spectrums.

rate of H_2 evolution, it can be concluded that the electrons generation, charge carriers transport, recombination of electron-hole pairs and surface reaction are all impact on the performance of photocatalysts.

It is well known that the electrons are important species in the process of H_2 production. Therefore, the performance of NO

removal was introduced to evaluate the activity of holes under simulated sunlight irradiation in the heterojunction with bridged structure and the results shown in Fig. 8. The removal rate of NO without the existence of photocatalyst and simulated sunlight irradiation are negligible (Fig. 8a), which indicated the NO removal is a photocatalytic process [51,52]. The removal rate of NO in moist con-

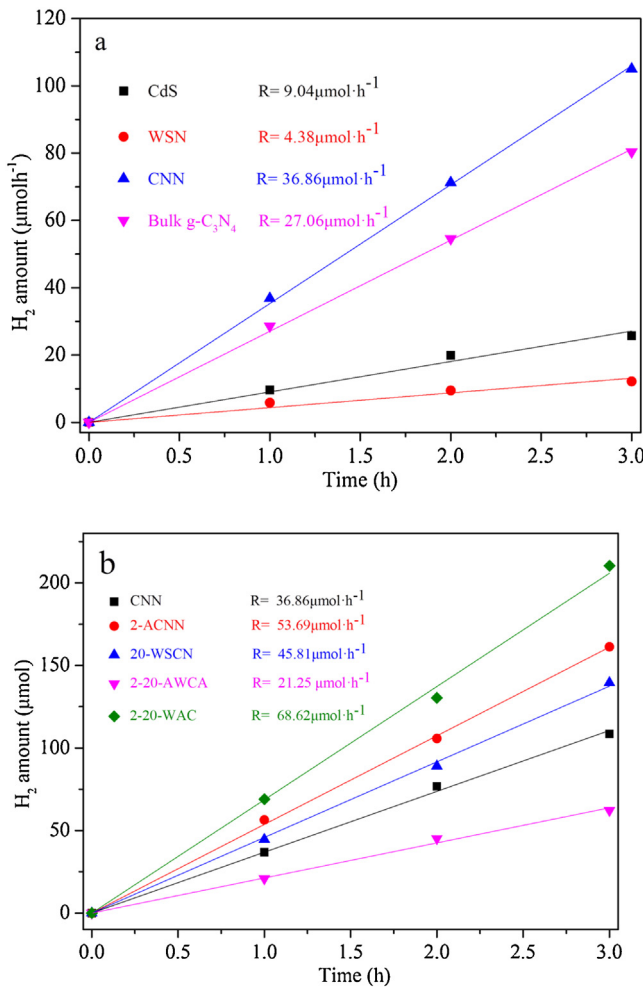


Fig. 7. The H₂ production with different catalysis (a) and different structure heterojunctions (b).

dition is higher than that in ambient condition, which can be owned to that the produced NO₂ can be absorbed by water molecules for the formation of nitric acid (3NO₂ + H₂O = 2HNO₃ + NO). Considering the HNO₃ can erosion the detectors and equipments, the performance of photocatalysts was evaluated in ambient condition. For 2-20-WAC sample, the concentrations of NO are decreased from 2.76 ppm to 0.82 ppm within 30 s simulated sunlight irradiation and then approached a steady state. The concentration curves of other samples are similar to that of 2-20-WAC. To view the performance of varies photocatalysts distinctly, the removal ratio was calculated and the results are shown in Fig. 8b. The 2-20-WAC is the most efficient samples and the removal ratio are reached 72.47% within 30 s irradiation, which is 3.70, 1.90, 1.17 and 1.32 times higher than that of CNN, 3-ACNN, 20-WSCN and 2-20-AWCA, respectively. The removal ability of x-ACNN are improved with the increase of Ag nanoparticles and the removal ratios of 1-ACNN, 2-ACNN, 3-ACNN are 20.28%, 24.59%, and 38.05%, respectively. The removal efficiency of y-WSCN are promoted with the increase of WSN and then decreased with the further additional. The removal ratio of NO with 10-WSCN, 20-WSCN, 30-WSCN are 56.60%, 62.02%, 51.33%, respectively. According to the results of NO removal, it can be concluded that the photocatalytic performance of heterojunctions with bridged structure are superiority than that with deposited structure.

To evaluate the reusability and stability of 2-20-WAC heterojunction, the five times circulation experiments are introduced and the experimental conditions are similar to that of hydrogen produc-

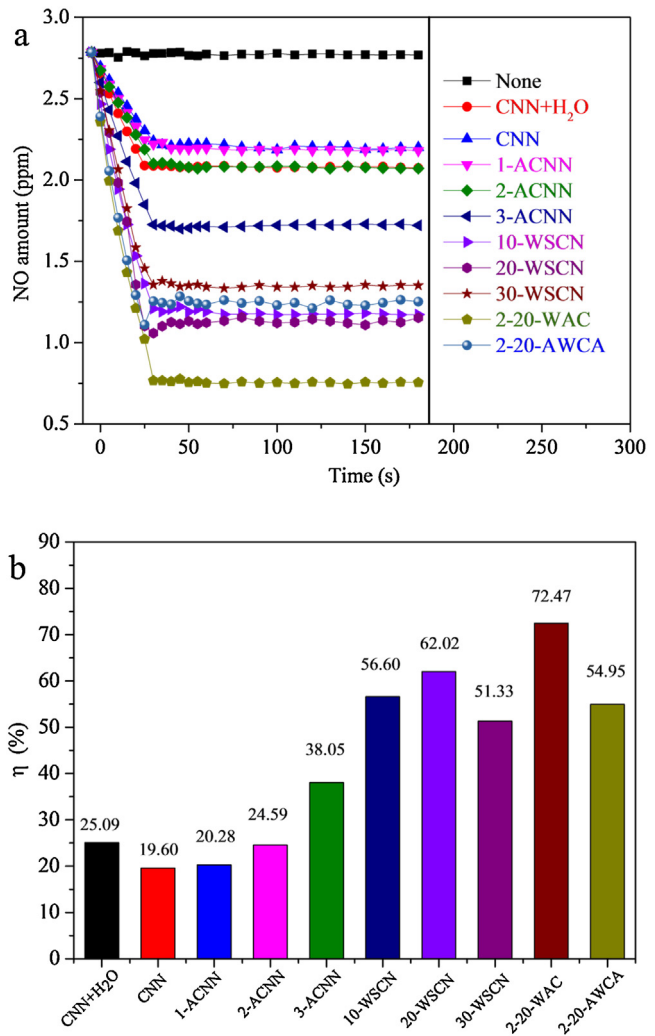


Fig. 8. The curves of NO amount (a) and NO removal rates (b) of different structure heterojunctions under simulated sunlight irradiation.

tion and NO removal process. The results can be seen in Fig. 9. The performance on H₂-production and NO removal are exhibited in Fig. 9a and b, respectively. It can be seen from Fig. 9a, the rate of H₂ production are decreased slightly in each circulation and the calculated value of H₂ production are 68.62 $\mu\text{mol} \cdot \text{h}^{-1}$, 64.74 $\mu\text{mol} \cdot \text{h}^{-1}$, 61.41 $\mu\text{mol} \cdot \text{h}^{-1}$, 58.79 $\mu\text{mol} \cdot \text{h}^{-1}$ and 57.19 $\mu\text{mol} \cdot \text{h}^{-1}$ in five times circulation. The value of the fifth circulation was decreased 16.66% compared to the first circulation, it can be attributed to the lost of photocatalyst in the washing process. The rate of H₂ production with 12 h continuously reaction was not decreased distinctly (in Fig.S7), which certified the as prepared 2-20-WAC sample are stabilized and can be recycling used. In Fig. 8b, it can be seen that the removal ratio of NO are decreased slowly with the circulation and the removal ratio are 72.47%, 71.93%, 70.53%, 69.42% and 68.56% from the first circulation to fifth circulation, respectively. The poor performance of 2-20-WAC in fifth circulation may be caused by the fact that the active sites of heterojunction were destroyed by the generated HNO₃.

3.3. Photocatalytic mechanism

It is well known that the high surface area and high separation efficiency of photo-generated electrons and holes are beneficial for the photocatalytic performance [15,53]. Fig. 10 shows the N₂ adsorption-desorption isotherms curves of bulk g-C₃N₄, CNN, 2-20-

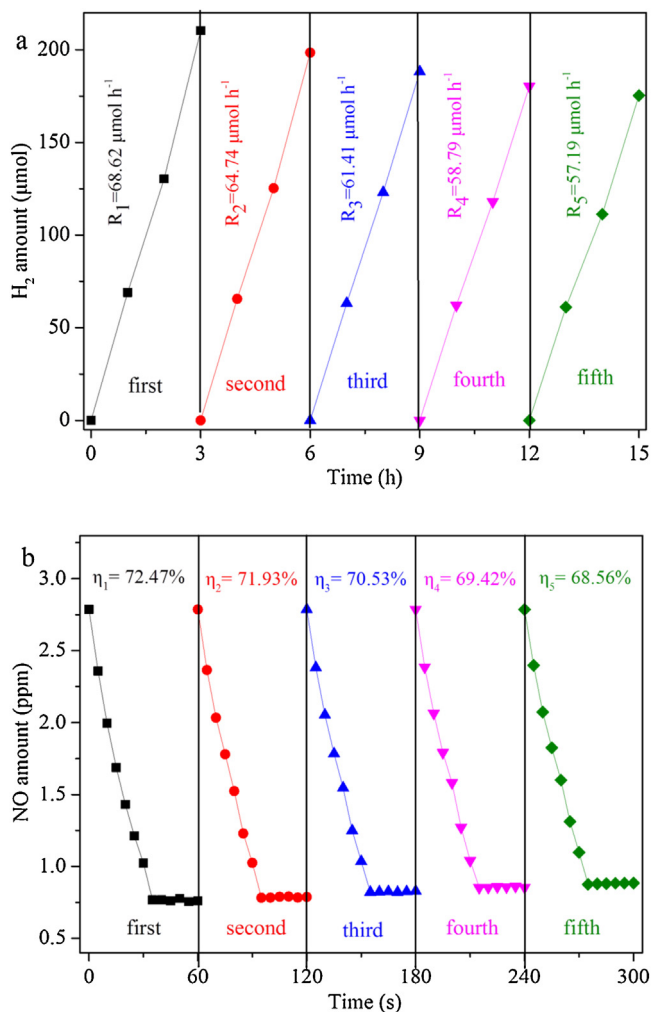


Fig. 9. The H₂ production rate (a) and the curves of NO amount (b) in 2-20-WAC samples circulation experiments.

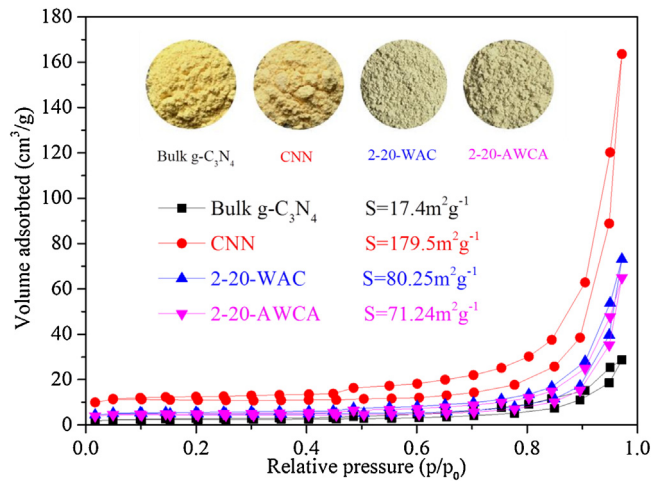


Fig. 10. The nitrogen adsorption–desorption isotherms curve.

WAC and 2-20-AWCA. The specific surface area of bulk g-C₃N₄ was 17.4 m² g⁻¹. However, the specific surface area of CNN is enlarged to 179.5 m² g⁻¹ after ultrasonic process, which is an ideal property for the adsorption of water molecules and NO molecules. Meanwhile, more active sites will be exposed with the increase of specific surface area, which can promote the photocatalytic performance in

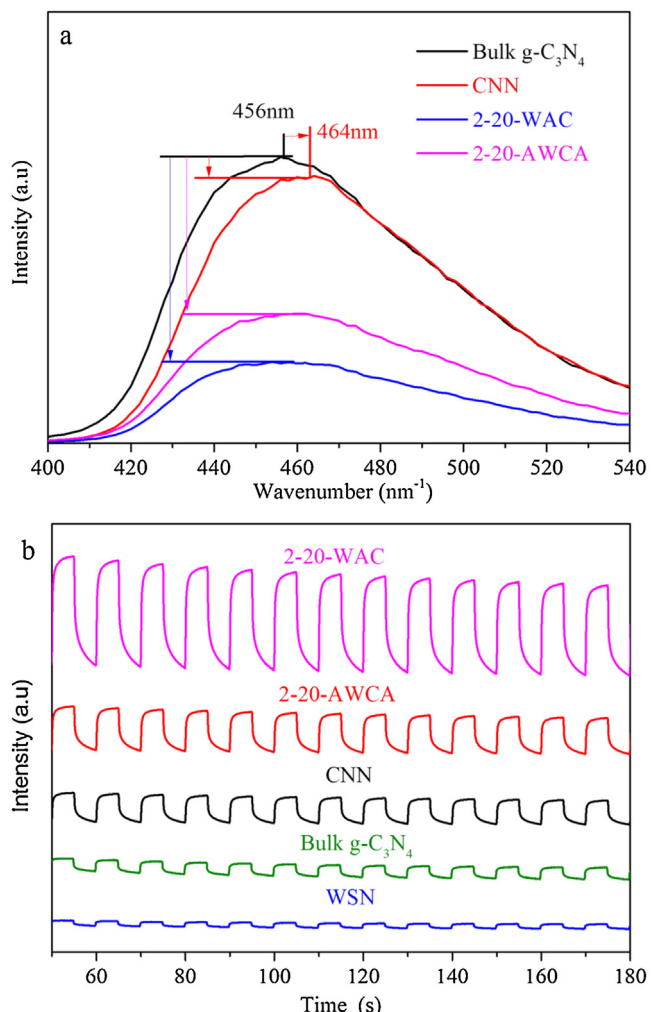


Fig. 11. The PL spectra (a) and photocurrent spectra (b).

theory. After the establishment of bridged structure and deposited structure, the specific surface area of 2-20-WAC and 2-20-AWCA are decreased to 80.25 m² g⁻¹ and 71.24 m² g⁻¹, respectively. Therefore, the bridged structure had a stronger adsorption property than that of deposited structure in theory. Meanwhile, the PL spectra and photocurrent signals are carried out to investigate the recombination rate and separation efficiency of electron-hole pairs (Fig. 11). The PL spectra of bulk g-C₃N₄, CNN, 2-20-AWCA and 2-20-WAC are displayed in Fig. 11a. For bulk g-C₃N₄, it can be found a strong emission peak at about 455 nm (excited by 275 nm), which can be owned to the recombination of exited electron-hole pairs. The peak intensity at 455 nm was decreased when the bulk g-C₃N₄ were exfoliated to CNN, which indicated that the recombination rate of exited electron-hole pairs was suppressed because of the quantum size effect of nanometer particles. For the heterojunctions of 2-20-AWCA and 2-20-WAC, both the intensity of them are lower than that of pure samples, which indicated that the heterojunctions can restrain the recombination of exited electron-hole pairs. Moreover, the intensity of 2-20-WAC is weaker than that of 2-20-AWCA at 455 nm, which revealed that the bridged structure can suppress the recombination of electron-hole pairs effectively. The intensity of photocurrent was also employed to investigate the exited electrons and the results shown in Fig. 11b. The photocurrent intensity of CNN is higher than that of bulk g-C₃N₄ and the intensity of WSN is the weakest one in the investigated pure samples. For heterojunctions, the photocurrent intensity of 2-20-WAC is higher than

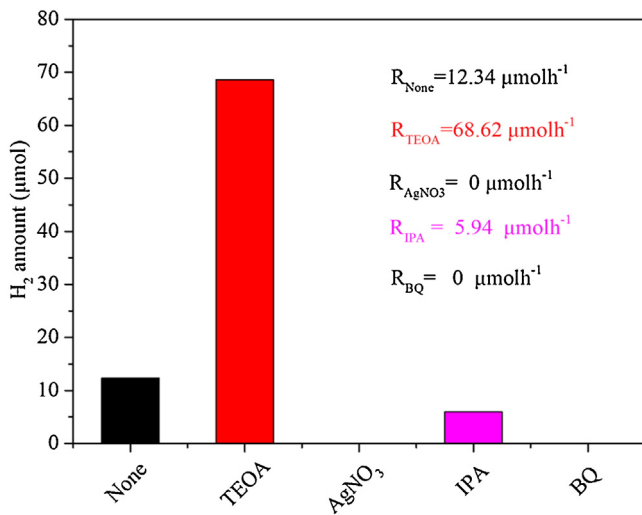


Fig. 12. The active species trapping experiments in H_2 production.

that of 2-20-AWCA and the intensity of them are much stronger than that of pure samples. Therefore, it can be concluded that the heterojunctions with bridged structure can promote the separation rate and suppress the recombination of electron-hole pairs at the same time.

In order to investigate the influence of various species on the process of H_2 generation in the heterojunction, the active species trapping experiments are employed. The different species are detected by adding TEOA (h^+ quencher), AgNO_3 (e^- quencher), IPA ($\cdot\text{OH}$ quencher) and BQ ($\cdot\text{O}_2^-$ quencher) into the photocatalytic system, respectively. Fig. 12 is the H_2 production rate with different scavengers. It can be seen that the rate of H_2 production was measured to $12.34 \mu\text{molh}^{-1}$ while any quenchers in the system. The H_2 production rate was decreased to $5.94 \mu\text{molh}^{-1}$ when the IPA ($\cdot\text{OH}$ quencher) introduced to the system, which revealed that the $\cdot\text{OH}$ species have a positive impact on the H_2 generation. The rate of H_2 evolution was increased to $68.62 \mu\text{molh}^{-1}$ after the TEOA (h^+ quencher) was introduced into the reactor, which indicated that the holes are the most suppress species in the H_2 production. It is interesting that there are no H_2 evolution in the system when the existence of AgNO_3 (e^- quencher) or BQ ($\cdot\text{O}_2^-$ quencher). According to above results and references [5,35,52], the process of H_2 generation and migration path of electrons can be explained in Eq. (1)–(5). The electrons were excited to the CB (conduction band) of samples while the simulated sunlight irradiated on the photocatalyst and the holes reserved in the VB (valence band) of semiconductors (Eq. (1)) [54]. The TEOA will be oxidized by the leaved holes in first equation (Eq. (2)) and the holes can also be attacked by OH^- (water splitting) for the formation of $\cdot\text{OH}$ special (Eq. (3)) [56]. The excited electrons can be summed up to three parts. The first part will return to the ground state with the release of energy and the second part will react with the dissolved oxygen for the formation of $\cdot\text{O}_2^-$ (Eq. (3)) [55]. The last part of excited electrons will be captured by the H^+ (dissociated from water molecules) and reduce them for H_2 production. However, the last part of excited electrons is the most effective ones in the process of H_2 generation and ratio of them is closely related to rate of H_2 production. Thus, restrain the recombination of electrons, accelerate the consumption of holes and decrease the dissolved oxygen are effective method to improve the performance of photocatalysts.

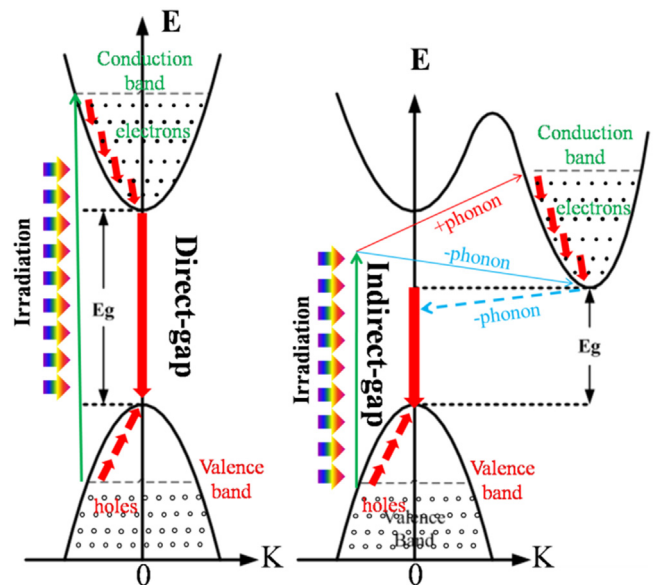
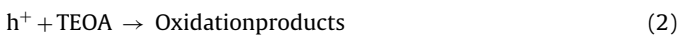


Fig. 13. The sketch map of direct-gap (left) and indirect-gap (right) materials.



According to reported, both the bulk $\text{g-C}_3\text{N}_4$ and WS_2 are indirect band gap semiconductors and the $\text{g-C}_3\text{N}_4$ and WS_2 nanosheets are direct band gap semiconductors inversely. The direct band gap properties are beneficial for the generation of photoinduced electrons and the fast recombination of charge carriers is also an obstacle for the performance of H_2 production and NO removal. The mechanism of photogenerated electrons in direct and indirect semiconductors are shown in Fig. 13. Based on above analysis, the enhancement mechanism for H_2 production and NO removal are proposed in Fig. 14 and the ideal model of heterojunction with bridged structure and deposited structure are shown in Fig. 15. The increased mechanism of H_2 production and NO removal of bridged structure can be ascribed to the effective transport of electrons and the restrained recombination of photo-induced electron-hole pairs (Fig. 14a). Specifically, the bridged structure had a stronger adsorptive property than that of deposited structure because it has a bigger specific surface area [50]. Therefore, the improvement mechanism can be explained by three perspectives. For the first, sufficient light will penetrate into each layer of the composites and the electrons of penetrated layers will be excited because the ultrathin structure of WSN and CNN. Thus, the sufficient excited electrons will be captured by the H^+ for the H_2 production and more reserved holes can remove NO effectively. Secondly, the interlayer distance was nearly expanded to the diameter of Ag nanoparticles (about 20 nm) because Ag nanoparticles intercalated into the interlayer of CNN and WSN. Therefore, more H_2O molecules and NO molecule will be adsorbed on the interface of composites to react with the generated electrons and holes in each layer of heterojunction. Thus, the performance on H_2 production and NO removal are improved distinctly. For the last ones, the bridged Ag nanoparticles can transport the electrons effectively and restrain the holes shifted to the adjacent layers. Herein, the excited electrons will transfer to Ag nanoparticles (SPR phenomenon, certified by the Raman spectra in Fig. S8) but the leaved holes will be eliminated by TEOA rapidly. Thus, the bridged structure can improve the separation efficiency and suppress the recombination of photo-induced electron-hole pairs at the same times. It can be illustrated the mechanism vividly in Fig. 14a. Besides, the bridged structure can offer more active sites (increased contact area) to split water for H_2 production or

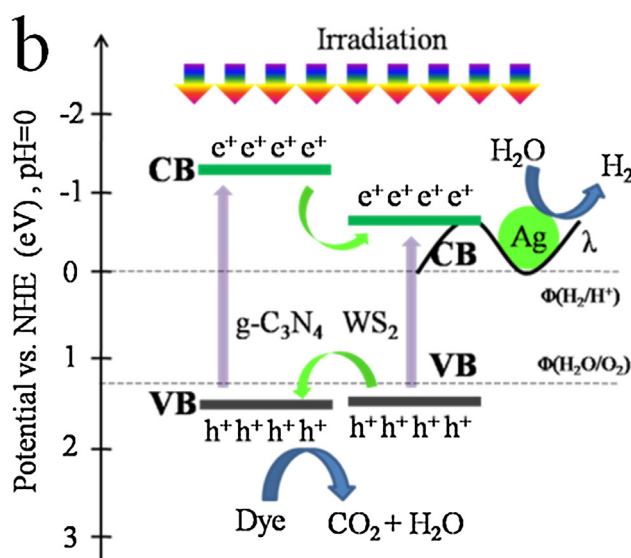
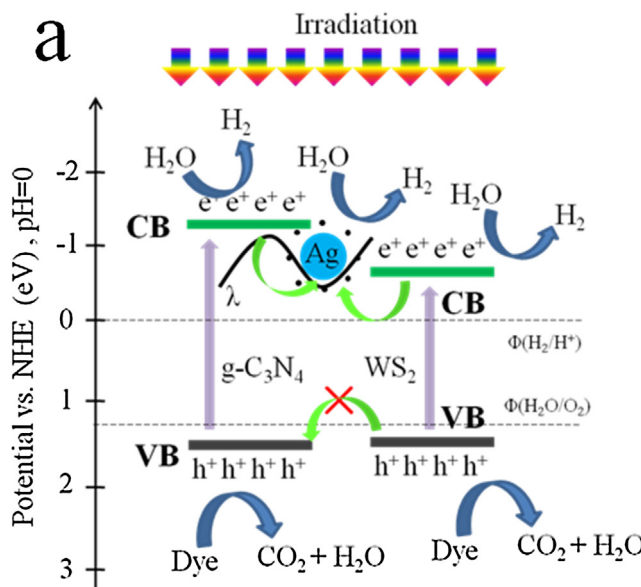


Fig. 14. The photocatalysis mechanism of 2-20-WAC (a) and 2-20-WAC (b) samples.

NO removal at the indoor air level. Differently, the deposited structure did not possess the mentioned properties compared to that of bridged structure and the mechanism were shown in Fig. 14b. To illustrate the mechanism specifically, the ideal model of 2-20-WAC and 2-20-AWCA are depicted in Fig. 15a and b, respectively. Therefore, the establishment of heterojunction with bridged structure is an effective project to improve the photocatalytic performance, which is also the best candidate to alleviate the energy shortage and eliminate the greenhouse gases emission.

4. Conclusion

The Ag nanoparticles bridged g-C₃N₄ and WS₂ nanosheets were prepared through a simple solvent evaporation and calcination process. The photocatalytic performance was significantly improved by the establishment of bridged structure and the optimum amount of Ag nanoparticles and WSN are 2% and 20% in mass fraction, respectively. The highest value of H₂ production and most effective removal ratio of NO with 2-20-WAC as photocatalyst could reached to 68.62 μmol h⁻¹ and 72.47%, respectively. In the H₂ gen-

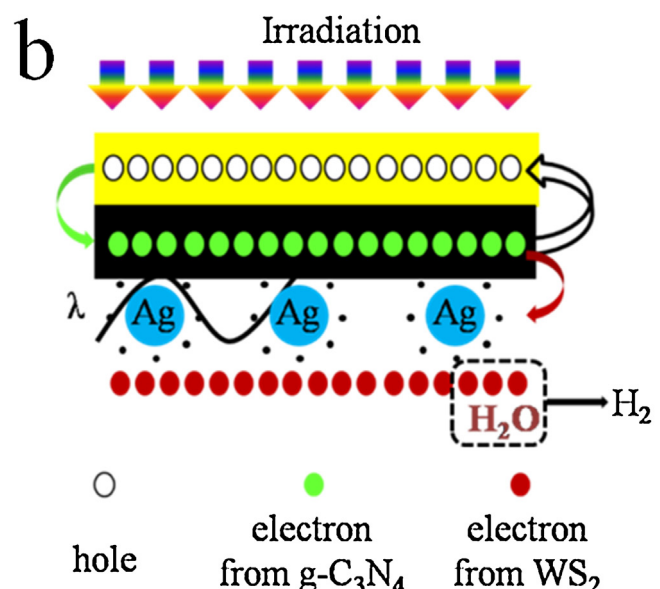
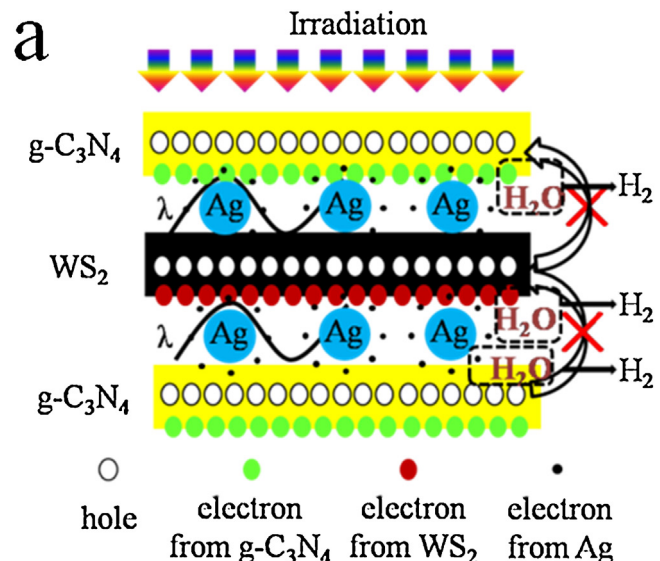


Fig. 15. The ideal models of 2-20-WAC (a) and 2-20-AWCA (b) samples.

eration process, the holes are the most obstacles and electrons are the most effective specials. The increased mechanism of bridged structure can be ascribed to the effective transport of electrons and restrained the recombination of photo-induced electron-hole pairs at the same time.

Acknowledgments

This work was supported by the National Natural Science Foundation of China (Nos. 21476183, 21676213, and 51372201), the Specialized Research Fund for the Doctoral Program of Higher Education of China (No. 20136101110009), the Project funded by China Postdoctoral Science Foundation (Nos. 2016M600809), the Project Supported by Natural Science Basic Research Plan in Shaanxi Province of China (Program No. 2017JM2026).

Appendix A. Supplementary data

Supplementary data associated with this article can be found, in the online version, at <http://dx.doi.org/10.1016/j.apcatb.2017.07.061>.

References

- [1] W.J. Ong, L.L. Tan, Y.H. Ng, S.T. Yong, S.P. Chai, *Chem. Rev.* 116 (2016) 7159–7329.
- [2] K. Chen, Z. Chai, C. Li, L. Shi, M. Liu, Q. Xie, Y. Zhang, D. Xu, A. Manivannan, Z. Liu, *ACS nano* 10 (2016) 3665–3673.
- [3] S. Cao, J. Yu, *J. Phys. Chem. Lett.* 5 (2014) 2101–2107.
- [4] Y. Kang, Y. Yang, L.C. Yin, X. Kang, L. Wang, G. Liu, H.M. Cheng, *Adv. Mater.* 28 (2016) 6471–6477.
- [5] D. Liu, J. Wang, X. Bai, R. Zong, Y. Zhu, *Adv. Mater.* 28 (2016) 7284–7290.
- [6] P. Zhang, T. Wang, J. Gong, *Adv. Mater.* 27 (2015) 5328–5342.
- [7] C. Liu, K.D. Dubois, M.E. Louis, A.S. Vorushilov, G. Li, *ACS Catal.* 3 (2013) 655–662.
- [8] R.O. Reithmeier, S. Meister, A. Siebel, B. Rieger, *Trans. Dalton* 44 (2015) 6466–6472.
- [9] Q. Zhang, Y. Huang, S. Peng, Y.F. Zhang, Z.X. Shen, J.J. Cao, W.K. Ho, S.C. Lee, D.Y.H. Pui, *Appl. Catal. B: Environ.* 204 (2017) 346–357.
- [10] L. Ye, D. Wang, S. Chen, *ACS Appl. Mater. Inter.* 8 (2016) 5280–5289.
- [11] J. Qin, J. Huo, P. Zhang, J. Zeng, T. Wang, H. Zeng, *Nanoscale* 8 (2016) 2249–2259.
- [12] C. Han, Y. Wang, Y. Lei, B. Wang, N. Wu, Q. Shi, Q. Li, *Nano Res.* 8 (2014) 1199–1209.
- [13] J. Sun, J. Zhang, M. Zhang, M. Antonietti, X. Fu, X. Wang, *Nat. Commun.* (2012) 1139.
- [14] L. Yin, Y.P. Yuan, S.W. Cao, Z. Zhang, C. Xue, *RSC Adv.* 4 (2014) 6127.
- [15] X. Bai, L. Wang, R. Zong, Y. Zhu, *J. Phys. Chem. C* 117 (2013) 9952–9961.
- [16] G. Dong, Y. Zhang, Q. Pan, J. Qiu, J. Photoch. Photobio. C 20 (2014) 33–50.
- [17] G. Gao, Y. Jiao, E.R. Waclawik, A. Du, *J. Am. Chem. Soc.* 138 (2016) 6292–6297.
- [18] Z. Zhao, Y. Sun, F. Dong, *Nanoscale* 7 (2015) 15–37.
- [19] W.J. Ong, L.L. Tan, S.P. Chai, S.T. Yong, *Trans. Dalton* 44 (2015) 1249–1257.
- [20] X.L. Wang, W.Q. Fang, Y.H. Li, P. Liu, H. Zhang, Y. Wang, P. Liu, Y. Yao, H. Zhao, H.G. Yang, *Int. J. Photoenergy* 2014 (2014) 1–8.
- [21] Z. Wang, W. Guan, Y. Sun, F. Dong, Y. Zhou, W.K. Ho, *Nanoscale* 7 (2015) 2471–2479.
- [22] J. Xu, L. Zhang, R. Shi, Y. Zhu, *J. Mater. Chem. A* 1 (2013) 14766–14772.
- [23] L. Huang, H. Xu, Y. Li, H. Li, X. Cheng, J. Xia, Y. Xu, G. Cai, *Trans. Dalton* 42 (2013) 8606–8616.
- [24] Y. Huang, Y.L. Liang, Y.F. Rao, D.D. Zhu, J.J. Cao, Z.X. Shen, W.K. Ho, S.C. Lee, *Environ. Sci. Technol.* 5 (2017) 2924–2933.
- [25] H. Zhang, G. Chen, D.W. Bahnemann, *J. Mater. Chem.* 19 (2009) 5089.
- [26] S. Qiao, H. Cao, X. Zhao, H. Lo, L. Zhuang, Y. Gu, J. Shi, X. Liu, H. Lai, *Int. J. Nanomed.* 10 (2015) 653–664.
- [27] R.C. Pawar, S. Kang, S.H. Ahn, C.S. Lee, *RSC Adv.* 5 (2015) 24281–24292.
- [28] K. Li, S. Gao, Q. Wang, H. Xu, Z. Wang, B. Huang, Y. Dai, J. Lu, *ACS Appl. Mater. Inter.* 7 (2015) 9023–9030.
- [29] S. Kumar, A. Baruah, S. Tonda, B. Kumar, V. Shanker, B. Sreedhar, *Nanoscale* 6 (2014) 4830–4842.
- [30] F.T. Li, Y. Zhao, Q. Wang, X.J. Wang, Y.J. Hao, R.H. Liu, D. Zhao, *J. Hazard. Mater.* 283 (2015) 371–381.
- [31] Z. Lou, C. Xue, *CrystEngComm* (2016).
- [32] M. Wang, S. Cui, X. Yang, W. Bi, *Talanta* 132 (2015) 922–928.
- [33] J. Zhang, Z. Zhu, X. Feng, *Chemistry* 20 (2014) 10632–10635.
- [34] J. Low, B. Cheng, J. Yu, M. Jaroniec, *Energy Storage Mater.* 3 (2016) 24–35.
- [35] J.M. Lee, E.K. Mok, S. Lee, N.S. Lee, L. Debbichi, H. Kim, S.J. Hwang, *Angew. Chem. Int. Edit.* 128 (2016) 8688–8692.
- [36] D. Voiry, H. Yamaguchi, J. Li, R. Silva, D.C. Alves, T. Fujita, M. Chen, T. Asefa, V.B. Shenoy, G. Eda, M. Chhowalla, *Nat. Mater.* 12 (2013) 850–855.
- [37] Z. He, W. Xu, Y. Zhou, X. Wang, Y. Sheng, Y. Rong, S. Guo, J. Zhang, J.M. Smith, J.H. Warner, *ACS Nano* 10 (2016) 2176–2183.
- [38] B. Zhu, H. Zeng, J. Dai, Z. Gong, X. Cui, *Proc. Nati. Acad. Sci. U.S.A.* 111 (2014) 11606–11611.
- [39] N. Peimyoo, J. Shang, C. Cong, X. Shen, X. Wu, E.K.L. Yeow, T. Yu, *ACS Nano* 7 (2013) 10985–10994.
- [40] M.S. Akples, J. Low, S. Wageh, A.A. Al-Ghamdi, J. Yu, J. Zhang, *Appl. Surf. Sci.* 358 (2015) 196–203.
- [41] Y. Hou, Y. Zhu, Y. Xu, X. Wang, *Appl. Catal. B: Environ.* 156–157 (2014) 122–127.
- [42] L. Zhang, X. Fu, S. Meng, X. Jiang, J. Wang, S. Chen, *J. Mater. Chem. A* 3 (2015) 23732–23742.
- [43] T. Xiong, W. Cen, Y. Zhang, F. Dong, *ACS Catal.* 6 (2016) 2462–2472.
- [44] G. Jiang, X. Li, M. Lan, T. Shen, X. Lv, F. Dong, S. Zhang, *Appl. Catal. B: Environ.* 205 (2017) 532–540.
- [45] J. Zhang, Y. Chen, X. Wang, *Energy Environ. Sci.* 8 (2015) 3092–3108.
- [46] X. Zhang, X. Xie, H. Wang, J. Zhang, B. Pan, Y. Xie, *J. Am. Chem. Soc.* 135 (2013) 18–21.
- [47] M.A. Lukowski, A.S. Daniel, C.R. English, F. Meng, A. Forticaux, R.J. Hamers, S. Jin, *Energy Environ. Sci.* 7 (2014) 2608.
- [48] W. Zhao, Y. Guo, S. Wang, H. He, C. Sun, S. Yang, *Appl. Catal. B: Environ.* 165 (2015) 335–343.
- [49] J. Zhang, M. Grzelczak, Y. Hou, K. Maeda, K. Domen, X. Fu, M. Antonietti, X. Wang, *Chem. Sci.* 3 (2012) 443–446.
- [50] C. Tang, E. Liu, J. Fan, X. Hu, Y. Ma, J. Wan, *RSC Adv.* 5 (2015) 91979–91987.
- [51] Z. Ni, F. Dong, H. Huang, Y. Zhang, *Catal. Sci. Technol.* 6 (2016) 6448–6458.
- [52] Q. Lu, Y. Yu, Q. Ma, B. Chen, H. Zhang, *Adv. Mater.* 28 (2016) 1917–1933.
- [53] Y.F. Li, A. Selloni, *ACS Catal.* 4 (2014) 1148–1153.
- [54] Z.Y. Wang, Y. Huang, W.K. Ho, J.J. Cao, Z.X. Shen, S.C. Shen, *Appl. Catal. B: Environ.* 199 (2016) 123–133.
- [55] F. Xu, X.N. Song, G.P. Sheng, H.W. Luo, W.W. Li, R.S. Yao, H.Q. Yu, *ACS Sustain. Chem. Eng.* 3 (2015) 1756–1763.
- [56] T.T. Zhang, C.Y. Zheng, W. Hu, W.W. Xu, H.F. Wang, *J. Appl. Phycol.* 22 (2009) 71–77.